Peridynamics-based large-deformation simulations for near-fault landslides considering soil uncertainty

Ruohan Wang[a,c], Shaofan Li[b], Yong Liu[c], Xuan Hu[b,*], Xin Lai[d], Michael Beer[a,e,f]

[a]*Institute for Risk and Reliability Leibniz University Hannover 30167 Hannover Germany*
[b]*Department of Civil and Environmental Engineering University of California Berkeley 94720 CA U.S.A.*
[c]*State Key Laboratory of Water Resources Engineering and Management Wuhan University Wuhan 430072 China*
[d]*Department of Engineering Structure and Mechanics Wuhan University of Technology Wuhan 430070 China*
[e]*Institute for Risk and Uncertainty and School of Engineering University of Liverpool Peach Street Liverpool L69 7ZF UK*
[f]*International Joint Research Center for Resilient Infrastructure & International Joint Research Center for Engineering Reliability and Stochastic Mechanics Tongji University Shanghai 200092 China*

Abstract

Landslides are widely acknowledged as among the most prevalent natural disasters. Peridynamics (PD), a mesh-free computational method, offers distinctive advantages in circumventing mesh distortion issues. However, limited attempts to employ PD in landslide simulation. Utilizing the features of non-ordinary state-based peridynamics (NOSBPD), we propose a computational method to analyze the entire process of slope run-out. Moreover, the occurrence and progression of landslides are notably affected by soil strength uncertainties. Hence, a coupling procedure is proposed to integrate random fields with NOSBPD, investigating the impact of spatial variability in soil strength on landslides. Results indicate that considering soil heterogeneity leads to a 12% increase in run-out distance compared to homogenous soil analyses. This highlights the significance of accounting for soil spatial variability to avoid underestimating landslide run-out distances. Additionally, this study compares the influence of ground motion types containing non-pulse ground motions and pulse-like ground motions (PLGMs) on entire landslide process. The findings suggest that landslides under PLGMs exhibit larger run-out distances and demonstrate a more concentrated spatial distribution, indicating higher susceptibilities to landslides under PLGMs. Lastly, we explored the interaction of two uncertainty sources on landslides. The findings can guide engineers in implementing assessments of potential uncertainties associated with landslides.
Keywords: Peridynamics, Run-out assessment, Landslide, Large-deformation simulation, Spatial

*corresponding author

Email addresses: ruohan.wang@irz.uni-hannover.de (Ruohan Wang), shaofan@berkeley.edu (Shaofan Li), liuy203@whu.edu.cn (Yong Liu), xuan_hu@berkeley.edu (Xuan Hu), laixin@whut.edu.cn (Xin Lai), beer@irz.uni-hannover.de (Michael Beer)

variability, Pulse-like ground motion

1. Introduction

Landslides are widely acknowledged as among the most prevalent natural disasters, posing a substantial risk to both human lives and property (Corominas et al., 2014; Wicki et al., 2020). Nowadays, computational approaches to slope stability analysis and slope failure pattern remain an active research field in geotechnical engineering, both in theory and in practice (Bui et al., 2011). This involves two most important aspects, the development of appropriate numerical tools and the accurate description of uncertainties.

When it comes to numerical tools, various methods have been proposed in the past decades. In early time, limiting equilibrium methods(LEM), which include the methods proposed by Fellenius (1936), Bishop (1955), Morgenstern and Price (1965), Janbu (1968), and Spencer (1967) played important roles in study of slope stability. Due to their simplicity and computational efficiency, LEMs have been widely appreciated by researchers and geotechnical engineers. However, the prior determination of critical slip surface, which is one of the crucial inputs of those methods may not always be available, especially when encountering complex conditions such as spatially non-uniform soil properties and multiple loading patterns, LEMs cannot always yield accurate predictions. Under this context, a more general computational framework was adopted in slope stability analysis, i.e., finite element method (FEM). FEM was formulated based on continuum mechanics. Once the local constitutive law of soil is properly determined, the location as well as shape of the critical slip surface can be computed automatically without making any assumptions in advance. In addition, FEM is compatible with the variation of soil mechanical properties, which has been demonstrated in the work done by Griffiths and Fenton (2004), Hicks and Li (2018), Liu et al. (2018). However, when it comes to large deformation and failure behavior of slopes such as landslides and collapses, numerical analysis carried out by FEM is hard to converge. The underlying reason is that the distorted mesh under large or even discontinuous deformation will cause severe numerical singularity problems. To address this issue, some adaptive re-meshing techniques were developed (see Bathe et al., 1975; Ghosh and Kikuchi, 1991; Hu and Randolph, 1998).

Alternatively, mesh-free methods have recently drawn great interests in research fields of geotechnical engineering. Since mesh-free methods describe problems at particle or material point scale, they can successfully avoid the mesh distortion problem and therefore be adopted in the large deformation or even failure study of slopes. Some representative mesh-free methods include the smoothed particle hydrodynamics (SPH) method (Gingold and Monaghan, 1977; Lucy, 1977), material point method (MPM) (Sulsky et al., 1994, 1995; Kularathna and Soga, 2017; Wang et al., 2018a) and peridynamics (PD) (Wang et al., 2016, 2018b, 2019). A lot of research has shown the applicability of using SPH or MPM in analyzing the stability problems of soil slopes under both static and dynamic loading patterns (Bui et al., 2007, 2008, 2011; Huang et al., 2020; Liu et al., 2021; Liu and Wang, 2021; Liu et al., 2022a; Xu and Stark, 2022; Zhang et al., 2022). However, to the best knowledge of the authors, only a few papers reported the application of PD in slope stability studies under merely gravity load (Lai et al., 2015; Zhang and Zhang, 2022). PD was initially proposed by Silling (Silling, 2000; Silling et al., 2007) as a non-local continuum theory. There are two distinct branches in PD, namely bond-based peridynamics(BBPD) and state-based peridynamics(SBPD). The SBPD, in particular, can derive the correspondence model, which is compatible with arbitrary constitutive relations in classic continuum mechanics such as Drucker-Prager model, and thus possesses the possibility to be applied directly in geotechnical problems. Despite the similarities between PD and SPH or MPM reported in previous literature (Zhou et al., 2021; Zeng et al., 2022), PD is somehow rarely applied in geotechnical problems compared with the other two. To the authors' best knowledge, no attempt has been made so far to adopt the SBPD theory in stability or run-out analysis of slope under dynamic loading such as earthquake.

Aside from numerical tools, accurate description of uncertainties is another crucial issue in slope stability analysis. One source of uncertainty arises from the soil heterogeneity. Natural soils are proven to exhibit spatial variability due to a range of factors, including geological sedimentation, weathering of natural soils, and chemical influences (Phoon and Kulhawy, 1999; Wang et al., 2021a; Li et al., 2023). Sedimentary processes within a given formation typically result in greater variation along vertical axis compared to horizontal axis (Zhang and Liu, 2020), which exerts a substantial influence on the stability and post-failure evolution behaviors. Due to technical limitations, the majority of prior investigations into soil heterogeneity have predominantly centered on small-strain analysis (e.g., Wang et al., 2020). Qu et al. (Qu et al., 2021) explored the impact of soil spatial variability on post-failure behavior based on MPM. However, current research has been limited in its exploration of large-deformation analysis based on PD. However, in large-deformation scenarios, adopting a uniform assumption for soil strength may result in non-conservative outcomes.

Besides, another source of uncertainty arises from the randomness of ground motions. As is well-known, the failure behavior of slopes is intimately linked to the ground motions. Currently, ground motions are primarily categorized into two types: non-pulse ground motions (NPGMs) and pulse-like ground motions (PLGMs). Near-fault PLGMs, known for their high amplitude and extended velocity record periods, have garnered significant attention since being reported by Housner and Hudson (Housner and Hudson, 1958). Numerous studies have delved into various aspects of this field, encompassing topics such as generation principles (Somerville et al., 1997), identification (Baker, 2007), simulation (Mavroeidis and Papageorgiou, 2003). However, the extent to which these two types of ground motions and the randomness of ground motions impact the landslide process remains unclear.

This study aims to propose a computational method to analyze the entire process of slope run-out by utilizing the features of PD. Besides, a novel coupling procedure is proposed to integrate random fields with PD with the ability to evaluate the run-out distance of a wide range of soil strength with spatial variability. The impacts of two distinct sources of uncertainty on landslides are examined: ground motion types, specifically NPGMs and PLGMs, and soil heterogeneity. To explore the relationship between run-out distances and heterogeneous properties, various random samples with different coefficients of variation are explicitly discussed. As a result, the coefficients of variation have remarkable effects on run-out distance and soil heterogeneity cannot be neglected in assessing landslide risk. This study also sheds light on the impact of the interaction between two sources of uncertainty on the landslide process and provides guidelines on implementing a more accurate assessment of the potential uncertainties associated with landslides.

2. Methodology

2.1. Non-ordinary state-based peridynamics

PD is a differential-integral and mesh-free approach based on the non-local averaging concept. It exhibits significant adaptability in handling discontinuity-related issues such as damage, cracks propagation, and fragments. PD contains two theories: BBPD and SBPD. Both theories offer different perspectives and modeling techniques. BBPD specifically focuses on the interactions and dynamics of bonds between material points. On the other hand, SBPD emphasizes the overall state and properties of the material points. One important trait of SBPD is its ability to establish correspondence models, which can link the particle states together with the classical continuum theories. Due to our aims of simulating system macro-scale time-history behaviors, we propose a computational method to analyze the entire process of slope run-out by utilizing the features of NOSBPD.

Unlike molecular dynamics and smoothed particle hydrodynamics, which utilize the updated Lagrangian approach, NOSBPD usually employs total Lagrangian approach in computing non-linear and failure behaviors of materialsBergel and Li (2016). This implies that the search of neighboring particles at each time step is not required in NOSBPD. According to the prevailing convention in continuum mechanics, under the assumption of Cartesian coordinates, variables containing subscripts 0 or capitalized subscripts (such as $\mathbf{X_I}$) are used to denote the quantities defined in reference (undeformed) configuration. Conversely, lowercase characters with lowercase subscripts (such as $\mathbf{x_i}$) are employed to represent quantities in a deformed configuration. Herein, all material mediums are assumed a non-local continuum. The schematic of NOSBPD is illustrated in Figure 1. Taking material particle $\mathbf{X}^A$ as an illustration, $\mathbf{X}^A$ exhibits interactions with adjacent particles within a distance denoted as δ. The zones in interaction distance are called 'horizon' (denoted as $\mathcal{H}_{\mathbf{X}^A}$ in this study). $\mathbf{X}^B$ represents the adjacent particles fall into $\mathcal{H}_{\mathbf{X}^A}$, where $B = 1, 2, 3, ..., n_a$ and $\boldsymbol{\xi}^{AB} = \mathbf{X}^B - \mathbf{X}^A$ is the bond vector. Note that the deformation state of the material particle is assessed through deformation state function $\mathbf{Y}\langle\cdot\rangle$, which is a local quantity.

The total free energy of $\mathbf{X}^A$ is expressed as a non-local integration of neighbor bond vectors within $\mathrm{H}_{\mathbf{X}^A}$,

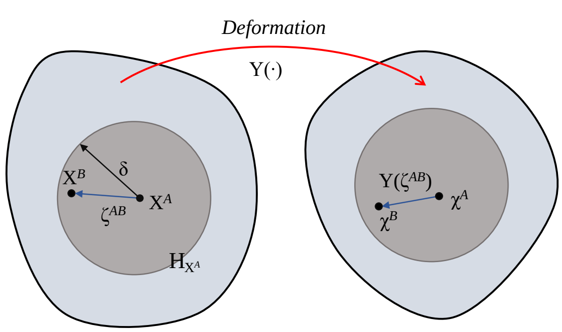

Figure 1: Schematic of NOSBPD.

$$\Phi(\mathbf{x}^A) = \int_{\mathcal{H}_{\mathbf{X}^A}} \phi(\mathbf{Y}^A\langle\boldsymbol{\xi}^{AB}\rangle, \mathbf{Y}^B\langle\boldsymbol{\xi}^{BA}\rangle)dV^B \tag{1}$$

where V^B is the volume of particle B falls into $\mathrm{H}_{\mathbf{X}^A}$; ϕ is the free energy per unit reference volume.

Based on the concept of bond, we can have $\boldsymbol{\xi}^{AB} = -\boldsymbol{\xi}^{BA}$.

Based on the principle of virtual work, the free energy of the material particle $\mathbf{X}^A$ can be expressed as,

$$\int_{\mathcal{H}_{\boldsymbol{X}^A}} \phi_{\mathbf{Y}^A}(\mathbf{Y}^A\langle\boldsymbol{\xi}^{AB}\rangle, \mathbf{Y}^B\langle\boldsymbol{\xi}^{BA}\rangle)\delta\mathbf{Y}^A(\boldsymbol{\xi}^{AB}) + \phi_{\mathbf{Y}^B}(\mathbf{Y}^A\langle\boldsymbol{\xi}^{AB}\rangle, \mathbf{Y}^B\langle\boldsymbol{\xi}^{BA}\rangle)\delta\mathbf{Y}^B\langle\boldsymbol{\xi}^{BA}\rangle dV^B = 0$$

where $\phi_{\mathbf{Y}^A} = \frac{\partial\phi}{\partial\mathbf{Y}^A} =: \mathbf{T}^A$ and $\phi_{\mathbf{Y}^B} = \frac{\partial\phi}{\partial\mathbf{Y}^B} =: \mathbf{T}^B$ are Gâteaux derivative of the total free energy function for $\mathbf{X}^A$ and $\mathbf{X}^B$.

Also, one can easily obtain that the virtual displacements $\delta\mathbf{Y}^B\langle\xi^{BA}\rangle = -\delta\mathbf{Y}^A\langle\xi^{AB}\rangle$. Then, a non-local integration could be utilized to represent the general variation form of linear momentum as follows,

$$\int_{\mathcal{H}_{\mathbf{X}^A}} \mathbf{T}^A\left[\mathbf{Y}^A\langle\boldsymbol{\xi}^{AB}\rangle, \mathbf{Y}^B\langle\boldsymbol{\xi}^{BA}\rangle\right] - \mathbf{T}^B\left[\mathbf{Y}^A(\boldsymbol{\xi}^{AB}), \mathbf{Y}^B\langle\boldsymbol{\xi}^{BA}\rangle\right] dV^B = 0 \tag{2}$$

where $\mathbf{T} = \phi_{\mathbf{Y}}\mathbf{Y}(\xi)$ is named as force state by Silling et al. (2007). On the other hand, the first law of thermodynamics requires

$$\delta\phi = \mathbf{P} : \delta\mathbf{F} \tag{3}$$

where $\mathbf{P}$ is the first Piola-Kirchhoff (PK-I) stress and $\mathbf{F}$ is non-local deformation gradient. Combining Cauchy-Born rule (Ren and Li, 2012), the deformed bond can be expressed as,

$$\mathbf{Y}(\boldsymbol{\xi}) = \mathbf{F}\cdot\boldsymbol{\xi} \tag{4}$$

The Cauchy-Born rule assumption establishes a connection between the non-local PD equation, denoted as Eq. 2, and the theory of local continuum mechanics. Evaluating $\mathbf{F}$ involves considering both the initial and changed horizons. According to previous studies regarding PD differential operator Madenci et al. (2016) and non-local differential operator Kan et al. (2021), the non-local deformation gradient can be computed by

$$\mathbf{F} = \mathbf{N}\cdot\mathbf{K}^{-1} \tag{5}$$

where the square matrix $\mathbf{N}$ writes as

$$\mathbf{N} = \sum_{B \in \mathcal{H}_{\mathbf{X}^A}} \omega(|\boldsymbol{\xi}|)\mathbf{Y}\langle\boldsymbol{\xi}\rangle \otimes \boldsymbol{\xi} V^B \tag{6}$$

and the invertible matrix $\mathbf{K}$ writes as

$$\mathbf{K} = \sum_{B \in \mathcal{H}_{\mathbf{X}^A}} \omega(|\boldsymbol{\xi}|)\boldsymbol{\xi} \otimes \boldsymbol{\xi} V^B \tag{7}$$

Assuming a sufficient number of particles exist within the horizon, the singularity of $\mathbf{K}$ and the ill-definition of $\mathbf{F}$ will not arise. The significance of Eq. 5 lies in its pivotal role in establishing the non-local deformation state at a specific material point. This equation can be used as an approximate deformation gradient in various constitutive relations to deduce stress measures, encompassing model.

Once stress is computed using these constitutive relations, for instance, stress measure $\mathbf{P}$, the connection between the force state $\mathbf{T}$ and stress measure $\mathbf{P}$ are straightforwardly deduced. Our subsequent focus will be on elucidating this connection through the lens of the principle of virtual work and we can derive the free energy density variation as,

$$\delta\Phi(\mathbf{x}^A) = \mathbf{P} : \delta\mathbf{F} = \mathbf{P} : \int_{H_{\mathbf{X}^A}} \omega(|\boldsymbol{\xi}|)\delta\mathbf{Y}(\boldsymbol{\xi}) \otimes \boldsymbol{\xi} \cdot \mathbf{K}^{-1} dV = \int_{\mathrm{H}_{\mathbf{X}^A}} \mathbf{T} \cdot \delta\mathbf{Y}(\boldsymbol{\xi}) dV \tag{8}$$

We can write it into discrete summation with indicial notations as

$$\sum_{B \in H_{\mathbf{X}^A}} \omega(|\boldsymbol{\xi}|) P_{iJ} \delta Y_i(\xi) \xi_K K_{KJ}^{-1} V^B = \sum_{B \in H_{\mathbf{X}^A}} T_i \delta Y_i(\boldsymbol{\xi}) V^B \tag{9}$$

Then, we can have stress measure and force state,

$$\mathbf{T} = \omega(|\boldsymbol{\xi}|)\mathbf{P}\mathbf{K}^{-1} \cdot \boldsymbol{\xi}, \quad \text{or} \tag{10}$$

$$T_i = \omega(|\boldsymbol{\xi}|) P_{iJ} \xi_K K_{KJ}^{-1} \tag{11}$$

2.2. Bond-associated deformation gradient

Zero-energy mode is a known problem in NOSBPD, which results from inaccurate approximation of the deformation gradient at bond level (Breitzman and Dayal, 2018; Chen, 2018). A common solution is to add penalty terms when computing the peridynamics force state, see work done by Breitenfeld et al. (2014); Bobaru et al. (2016); Li et al. (2018); Tupek and Radovitzky (2014); Yaghoobi and Chorzepa (2017). However, the choice of penalty terms and their magnitudes usually depends on researchers' experience and trial-and-error process. Chen and Hu (2023) proposed a novel method to compute the bond-associated deformation gradient. The core idea of the method is to apply a biased weight function instead of traditional step kernel, Gaussian kernel or polynomial kernel in Eq. 6 and Eq. 7. The biased weight function for bond $\boldsymbol{\xi}$ is defined as

$$\omega_{\xi}(\boldsymbol{\xi}, \boldsymbol{\xi'}) = \exp\left(-m_1 \frac{||\boldsymbol{\xi}'| - |\boldsymbol{\xi}||}{\xi}\right) \left(\frac{1}{2} + \frac{1}{2}\cos(\widehat{\boldsymbol{\xi}\boldsymbol{\xi}'})\right)^{m_2} \tag{12}$$

where $\boldsymbol{\xi'}$ is a bond between the center particle and its arbitrary neighboring particle; the symbol $\widehat{\cdot}$ indicates the angle between two bonds; the symbol $|\cdot|$ refers to the Euclidean norm; and m_1, m_2 are two controlling parameters, which are adopted as $m_1 = 3, m_2 = 3$ respectively. Consequently, Eq. (5), Eq. (6) and Eq. (7) should be rephrased as

$$\mathbf{F}_{\boldsymbol{\xi}} = \mathbf{N}_{\boldsymbol{\xi}} \cdot \mathbf{K}_{\boldsymbol{\xi}}{}^{-1} \tag{13}$$

$$\mathbf{N}_{\boldsymbol{\xi}} = \sum_{B \in \mathcal{H}_{\mathbf{X}^A}} \omega_{\xi}(\boldsymbol{\xi}, \boldsymbol{\xi'}) \mathbf{Y}\langle\boldsymbol{\xi}\rangle \otimes \boldsymbol{\xi} V^B \tag{14}$$

$$\mathbf{K}_{\boldsymbol{\xi}} = \sum_{B \in \mathcal{H}_{\mathbf{X}^A}} \omega_{\xi}(\boldsymbol{\xi}, \boldsymbol{\xi'}) \boldsymbol{\xi} \otimes \boldsymbol{\xi} V^B \tag{15}$$

It has been demonstrated that this method can measure the deformation gradient at bond level accurately. Therefore, the zero-energy problem in NOSBPD does not exist anymore.

2.3. Failure criteria

This paper uses two criteria to evaluate failure: bond failure and particle failure. Bond failure occurs when the length of the deformed bond surpasses a critical threshold. The deformation of bond is measured by a scalar quantity that is defined as

$$s := \frac{|\mathbf{Y}(\boldsymbol{\xi})| - |\boldsymbol{\xi}|}{|\boldsymbol{\xi}|} \tag{16}$$

The certain threshold, which is usually referred to as 'critical bond stretch' is given by Bobaru et al. (2016) as:

$$s_0 := \begin{cases} \sqrt{\frac{5G_c}{9\kappa\delta}}, & \text{3D case} \\ \sqrt{\frac{\pi G_c}{3\kappa'\delta}}, & \text{2D case} \\ \sqrt{\frac{3G_c}{E\delta}}, & \text{1D case} \end{cases} \tag{17}$$

where G_c is the energy release rate of materials; δ is the radius of the peridynamics horizon; $\kappa := E/(3(1-2\nu))$ refers to the bulk modulus for three dimensional problem; $\kappa' = E/(2(1-\nu))$ is the bulk modulus for plane stress problem while $\kappa' = E/(2(1-\nu-2\nu^2))$ for plane strain problem; and E is the Young's modulus of the material. Once $s \geq s_0$ is satisfied, the bond will be broken and the interactive forces will no longer be calculated.

To improve the numerical stability, the particle failure criterion is used along with bond failure criterion. Before computing the nonlocal deformation gradient, the $\mathbf{K}_{\boldsymbol{\xi}}$ matrix given in Eq.15 should be verified for its invertibility. The $\mathbf{K}_{\boldsymbol{\xi}}$ matrix is derived from the unbroken bonds within the horizon of each particle. If the matrix is singular, it implies that the particles have very few intact bonds left and this particle should be considered as a failed particle with zero force state. If $\mathbf{K}_{\boldsymbol{\xi}}$ is invertible, then the determinant of $\mathbf{F}_{\boldsymbol{\xi}}$ shall be checked. It is known that $\det(\mathbf{F}_{\boldsymbol{\xi}})$ corresponds to the change of volume of the particle, and a negative value indicates the particle has a negative volume, which is physically impossible. In this sense, if $\det(\mathbf{F}_{\boldsymbol{\xi}}) < 0$, then the particle should also be marked as failed and excluded from force computation process.

2.4. Drucker-Prager plastic model

The NOSBPD has the merit of integrating the constitutive models to assess the effective stresses. It is well-known that soil material is highly intricate and complex so the response of soil behavior under seismic loading exhibits highly nonlinear characteristics. Nowadays, Drucker-Prager (DP) plastic model has been widely utilized in simulating the nonlinear characteristics of soils in geotechnical fields (Fan et al., 2016, 2021; Lai et al., 2015). Therefore, we incorporated DP plastic model into NOSBPD in order to establish the yield surface of the soil and the general DP yield function can be written as,

$$\begin{cases} f = \|\mathbf{s}\| - (A^{\varphi}c^{'} - B^{\varphi}p^{'}) \leq 0 \\ A^{\varphi} = \frac{2\sqrt{6}\cos\varphi^{'}}{3+\beta\sin\varphi^{'}} \\ B^{\varphi} = \frac{2\sqrt{6}\sin\varphi^{'}}{3+\beta\cos\varphi^{'}}, -1 \leq \beta \leq 1 \end{cases} \tag{18}$$

where $\mathbf{s}$ denotes deviatoric stress tensor; p' is mean hydrostatic pressure; c' denotes effective cohesion; φ' is effective friction angle. Specifically, the DP model is close to triaxial extension (TE) corner of Mohr-Coulomb (MC) yield surface if $\beta = 1$; and that close to triaxial compression (TC) corner if $\beta = -1$. Then, the non-associative plastic potential function is expressed as,

$$\begin{cases} g = \|\mathbf{s}\| - (A^{\phi}c^{'} - B^{\phi}p^{'}) \\ A^{\phi} = \frac{2\sqrt{6}\cos\phi^{'}}{3+\beta\sin\phi^{'}} \\ B^{\phi} = \frac{2\sqrt{6}\sin\phi^{'}}{3+\beta\cos\phi^{'}}, -1 \leq \beta \leq 1 \end{cases} \tag{19}$$

where ϕ' is effective dilation angle.

The Helmholtz free energy function $\rho_s\Phi$ per unit deformed soil skeleton volume consists of the elastic component and plastic component as,

$$\rho_s\Phi(\boldsymbol{\epsilon}^e, \boldsymbol{\zeta}) = \frac{1}{2}\boldsymbol{\epsilon}^e : \mathbf{D}^e : \boldsymbol{\epsilon}^e + \frac{1}{2}\boldsymbol{\zeta} \cdot \mathbf{H} \cdot \boldsymbol{\zeta} \tag{20}$$

where $\boldsymbol{\epsilon}^e$ denotes elastic strain tensor; $\mathbf{D}^e$ is elastic modulus tensor; $\mathbf{H}$ denotes hardening or softening modulus matrix and $\boldsymbol{\zeta}$ is a parameter related to internal state variables.

Based on Eq. 20, we can have the expressions of stress and internal state variable as,

$$\dot{\boldsymbol{\sigma}}' = \frac{\partial(\rho_s\Phi)}{\partial\dot{\boldsymbol{\zeta}}} = \mathbf{D}^e : \dot{\boldsymbol{\epsilon}}^e = \mathbf{D}^e : (\dot{\boldsymbol{\epsilon}} - \dot{\boldsymbol{\epsilon}}^p) \tag{21}$$

$$\dot{\mathbf{q}}^{\zeta} = \frac{\partial\rho_s\Phi}{\partial\dot{\boldsymbol{\zeta}}} = \mathbf{H} \cdot \dot{\boldsymbol{\zeta}} \tag{22}$$

where $\dot{\mathbf{q}}^{\zeta} = \{c', \varphi', \phi'\}^T$, is a stress-like internal state variable. Besides, the hardening or softening modulus matrix can be calculated as,

$$\mathbf{H} = \begin{bmatrix} H^c & 0 & 0 \\ 0 & H^\varphi & 0 \\ 0 & 0 & H^\Phi \end{bmatrix} \tag{23}$$

where H^c, H^φ, H^Φ are hardening or softening moduli. Based on the non-associative plastic potential function, we can have

$$\dot{\boldsymbol{\epsilon}}^p = \dot{\gamma}\frac{\partial g}{\partial \boldsymbol{\sigma'}} = \dot{\gamma}(\frac{\partial \|s\|}{\partial \boldsymbol{\sigma'}} + B^\Phi \frac{\partial p'}{\partial \boldsymbol{\sigma'}}) = \dot{\gamma}(\hat{\mathbf{n}} + \frac{1}{3}B^\Phi \Pi) \tag{24}$$

where $\hat{\mathbf{n}}$ denotes the normal vector for $\mathbf{s}$. Here, $\mathbf{s}$ is the deviatoric stress and we can have that $\hat{\mathbf{n}} = \frac{\mathbf{s}}{\|\mathbf{s}\|}$. Π denotes the second-order identity tensor. Also, the evolution of the stress-like internal state variable $\dot{\mathbf{q}}$ is written as,

$$\dot{\mathbf{q}}^\zeta = \mathbf{H} \cdot \dot{\boldsymbol{\zeta}} = \dot{\gamma}\mathbf{H} \cdot \mathbf{h}(\boldsymbol{\sigma}, \mathbf{q}^\zeta). \tag{25}$$

From the principle of maximum plastic dissipation, the hardening function $\mathbf{h}$ can be derived as,

$$\mathbf{h} = -\frac{\partial f}{\partial \mathbf{q}^\zeta} \tag{26}$$

due to

$$\frac{\partial f}{\partial \phi'} = 0, \tag{27}$$

and we also have

$$h^\phi = -\frac{\partial g}{\partial \phi'}, \tag{28}$$

Based on Eqs. 26 - 28, we can rewrite the hardening function $\mathbf{h}$ as,

$$\mathbf{h} = \begin{pmatrix} A^\varphi \\ \frac{\partial A^\varphi}{\partial \varphi'}c' - \frac{\partial B^\varphi}{\partial \varphi'}p' \\ \frac{\partial A^\Phi}{\partial \Phi'}c' - \frac{\partial B^\Phi}{\partial \Phi'}p' \end{pmatrix} \tag{29}$$

The plastic multiplier $\dot{\gamma}$ is calculated by

$$\dot{\gamma} = \frac{1}{\chi}\frac{\partial f}{\partial \boldsymbol{\sigma'}} : \mathbf{D}^e : \dot{\boldsymbol{\epsilon}}, \tag{30}$$

and

$$\chi = \frac{\partial f}{\partial \boldsymbol{\sigma}'} : \mathbf{D}^e : \frac{\partial g}{\partial \boldsymbol{\sigma}'} - \frac{\partial f}{\partial \mathbf{q}^\zeta} : \mathbf{H} \cdot \mathbf{h}. \tag{31}$$

Eqs. 21, 22, 30 and 31 are the equations to update and calculate the increments of nonlinear elastoplastic DP constitutive relationship. To solve the system of equations, one way is to utilize Newton–Raphson method. More details on Newton–Raphson method can be found in references (Ypma, 1995; Akram and Ann, 2015).

$$\boldsymbol{\sigma}_{n+1}^{',tr} = \boldsymbol{\sigma}_n^{'} + \mathbf{D}^e : \Delta\boldsymbol{\epsilon} \tag{32}$$

$$f_{n+1}^{tr} = \left\|\mathbf{s}^{tr}\right\| - \left(A^{\varphi n} c_n' - B^{\varphi n} (p')_{n+1}^{tr}\right. \tag{33}$$

where f_{n+1}^{tr} is an index to determine if the material has entered the yielding stage; when $f_{n+1}^{tr} < 0$, the material is still in the elastic phase. Then we can have $\boldsymbol{\sigma}_{n+1}^{'} = \boldsymbol{\sigma}_{n+1}^{',tr}$; $\mathbf{q}_{n+1}^{\zeta} = \mathbf{q}_n^{\zeta}$. When $f_{n+1}^{tr} \geq 0$, the material enters the plastic phase and we can obtain the expressions of $\Delta\gamma$, $\boldsymbol{\sigma}'_{n+1}$ and $\mathbf{q}_{n+1}^{\zeta}$ as,

$$\Delta\gamma = \frac{f_{n+1}^{tr}}{2\mu + KB^{\varphi}B^{\Phi} + H^c \left(A^{\varphi}\right)^2} \tag{34}$$

$$\boldsymbol{\sigma}'_{n+1} = \boldsymbol{\sigma}_{n+1}^{',tr} - \Delta\gamma(KB^{\Phi}\Pi + 2\mu\hat{\mathbf{n}}_{n+1}) \tag{35}$$

$$\mathbf{q}_{n+1}^{\zeta} = \mathbf{q}_n^{\zeta} + \Delta\gamma\mathbf{H} \cdot \mathbf{h}(\boldsymbol{\sigma}, \boldsymbol{q}^{\zeta}) \tag{36}$$

Combining with Hughes-Winget algorithm, we can obtain a nonlinear formula that could break free from the constraints of small deformation assumptions, which is the foundation of large-deformation analysis. More details and applications of Hughes-Winget algorithm can be found in references (Liu et al., 2022b; Staubach et al., 2023).

$$\mathbf{x}_{n+\alpha} = (1-\alpha)\mathbf{x}_n + \alpha\Delta\mathbf{u} \tag{37}$$

Equation 5 represents the PD expression for the first derivative of x in reference configuration $\mathbf{X}$. Also, the deformation gradient in the current configuration $x_{n+\alpha}$ should be written into,

$$\mathbf{F}_{n+\alpha} = \frac{\partial \mathbf{x}_{n+\alpha}}{\partial \mathbf{X}} = (\sum_{B \in H_{\mathbf{X}^A}} \omega(|\boldsymbol{\xi}|)(\mathbf{x}^B_{n+\alpha} - \mathbf{x}^A_{n+\alpha}) \otimes \boldsymbol{\xi} \cdot \mathbf{K}^{-1} \tag{38}$$

Also, the gradient $\Delta\mathbf{u}$ in $\mathbf{X}$ is expressed as,

$$\mathbf{C} = \frac{\partial(\Delta\mathbf{u})}{\partial \mathbf{X}} = (\sum_{B \in H_{\mathbf{X}^A}} \omega(|\boldsymbol{\xi}|)(\Delta\mathbf{u}^B - \Delta\mathbf{u}^A) \otimes \xi) \cdot \mathbf{K}^{-1} \tag{39}$$

Then, following the chain rule, Δu in $x_{n+\alpha}$ is written as,

$$\mathbf{G} = \frac{\partial(\Delta\mathbf{u})}{\partial \mathbf{x}_{n+\alpha}} = \mathbf{C} \cdot \mathbf{F}^{-1}_{n+\alpha} \tag{40}$$

where $\mathbf{G}$ is deformation gradient increment which is consisted with strain $\boldsymbol{\gamma}$ and rotation $\boldsymbol{\omega}$ increments,

$$\boldsymbol{\gamma} = \frac{1}{2}(\mathbf{G} + \mathbf{G}^T) \tag{41}$$

$$\boldsymbol{\omega} = \frac{1}{2}(\mathbf{G} - \mathbf{G}^T) \tag{42}$$

The objective effective stress increment is expressed by,

$$\Delta\boldsymbol{\sigma}' = \mathbf{D}^e : \boldsymbol{\gamma} \tag{43}$$

Then, we can derive the constitutive update Equation 32 into,

$$\boldsymbol{\sigma}'_{n+1} = \hat{\boldsymbol{\sigma}}'_n + \Delta\boldsymbol{\sigma}' \tag{44}$$

$$\hat{\boldsymbol{\sigma}}'_n = \mathbf{R}^T \cdot \boldsymbol{\sigma}'_n \cdot \mathbf{R} \tag{45}$$

$$\mathbf{R} = \Pi + (\Pi - \alpha\boldsymbol{\omega})^{-1} \cdot \boldsymbol{\omega} \tag{46}$$

2.5. Validation of NOSBPD algorithm

To validate the NOSBPD algorithm, two typical cases are selected to perform. The first validation case is to simulate the failure process of a soil slope under gravity and with homogeneous soil. The slope has a horizontal base length of 45 meters, a height of 15 meters, and a crest length of 12 meters. The left and right boundaries are characterized by free-roller boundary conditions, whereas the bottom exhibits complete fixity. The soil mechanical parameters are listed in Table 1. For more details regarding the modelling information about the slope, readers are referred to Bui et al. (2011).

Figure 2 depicts the contour of slip surface for validation case by NOSBPD (white band), compared with the results obtained by SPH method (red dashed line) (Bui et al., 2011) and also limit equilibrium critical slip surface (solid line). It can be found that the critical slip surface obtained by NOSBP is close enough to the one determined by limit equilibrium analysis, which demonstrates the effectiveness and reliability of NOSBPD. Furthermore, NOSBPD results fall within a similar range to those obtained through SPH calculations, further confirming the efficacy of the NOSBPD algorithm in simulating slip surfaces. It should be noted that the NOSBPD can provide a narrower, more distinct prediction of the slip surface when compared with the results obtained from finite element analysis. In conclusion, the first case study demonstrates the capability of NOSBPD in capturing the critical sliding surface of a soil slope under gravitational loading.

Table 1: Soil mechanical parameters of validation case.

Mechanical parameter	Symbol	Unit	Value
Young's modulus	E	MPa	100
Density	ρ	g/cm^3	2
Poisson's ratio	μ	-	0.3
Friction angle	φ	$(^\circ)$	20
Dilatancy angle	ψ	$(^\circ)$	9
Cohesion	c	kPa	10
Slope height	H	m	10
Slope angle	α	$(^\circ)$	26.6

To further validate our NOSBPD algorithm, the second validation case is a large-deformation collapse process of a sand column after releasing the right boundary. As depicted in Figure 3, the sand column has dimensions of 50 mm $\times$ 50 mm. Validation simulation is based on the physical experiment data by Shi et al. (2018), while they also conducted numerical simulations by MPM method. In the current parameter selection, we have maintained consistency with their parameters, with cohesion set to 0 kPa and the friction angle set at 35°. The density of soil is 1,450 kg/m^3, Poisson's ratio is 0.31, and Young's modulus is 2.6 MPa. The simulation

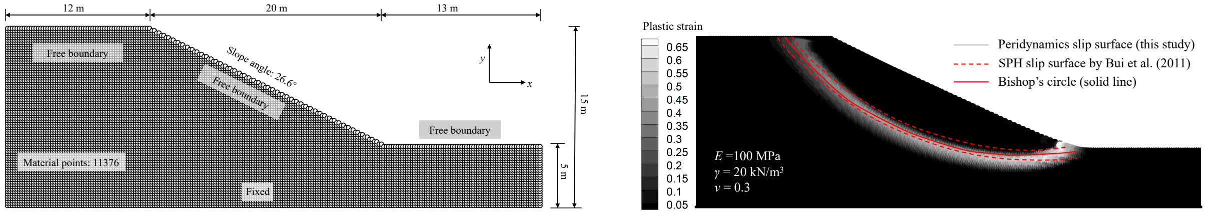

(a) (b)

Figure 2: Validation case. (a) Schematic of geometry and boundary conditions. (b) Contour of slip surface by NOSBPD (white band), compared with the results obtained by SPH method (red dashed line) and also limit equilibrium critical slip surface (solid line).

boundaries are set the same as in Shi et al.'s study. In PD, dealing with contact is a complex task Mohajerani and Wang (2022). However, by using the approach outlined by Huang et al. (2020), we can simplify the interaction between particles and ground by treating it as particle-to-rigid body contact type. This means the displacements and velocities of particles in z direction will be adjusted if their z-coordinates are negative. The self-contact problem between particles is neglected in this study though, as it is not considered a significant factor in slope run-out problem and this way computational efficiency can be improved greatly.

The deformation profile of sand column after releasing the right boundary at $t = 40$ ms, $t = 80$ and $t = 320$ ms is depicted in Figure 4, including the results from NOSPBD (this study), physical experiment (dashed line), and MPM (Shi et al., 2018). After releasing the right boundary, the deformation profile of sand column at $t = 40$ ms, $t = 80$ ms and $t = 320$ ms is depicted in Figure 4, including the results from NOSPBD (this study), physical experiment (dashed line), and MPM (Shi et al., 2018). It can be observed that the current NOSPBD algorithm successfully simulates the collapse process of the sand column, and the deformation profile obtained by NOSBPD closely resembles that of the physical experiment, outperforming the MPM simulation results. This indicates that the current NOSBPD algorithm exhibits reliable performance.

2.6. NOSBPD modeling of landslides

In this study, we aim at demonstrating the capability of the proposed computational method in simulating landslide problems. The geometry as well as boundary conditions of the model is depicted in Figure 5. The constructed slope model has dimensions of 60 meters in length, 10 meters in height, and a slope angle of 26.6 degrees with a total of 2047 material points. The side boundaries are characterized by normal restrictions, while the bottom boundary is fully fixed. The model adopts free boundaries for the other conditions. The entire slope model is subjected

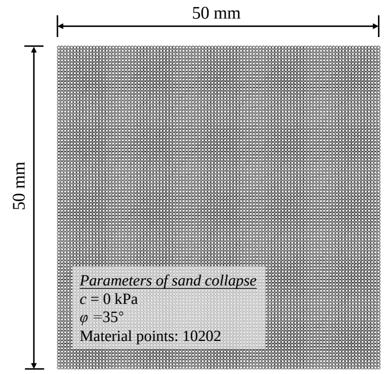

Figure 3: Geometry and modeling details of validation case.

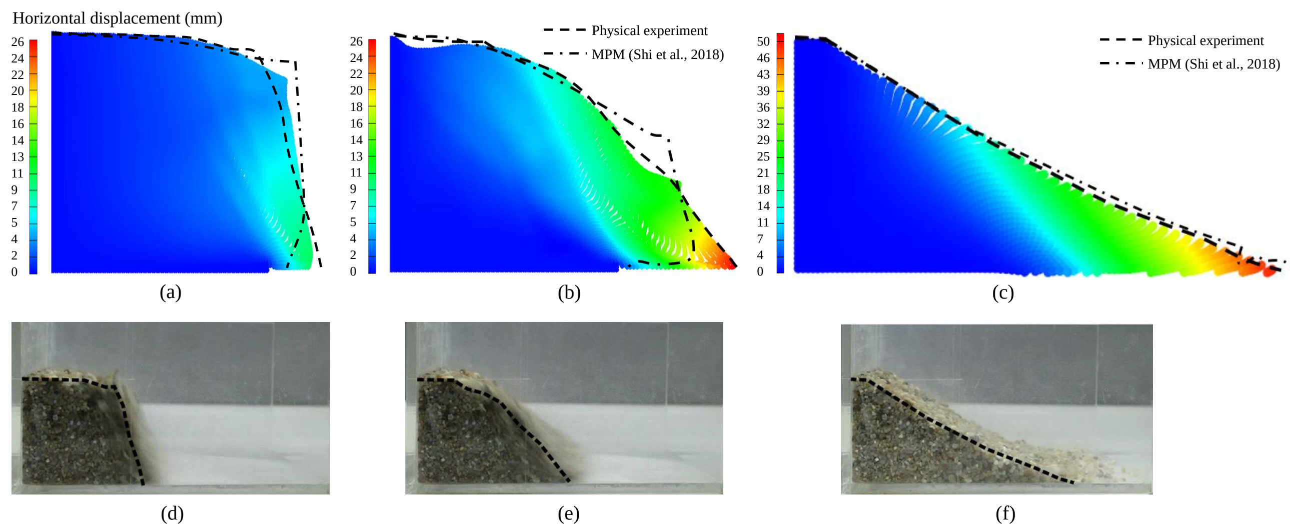

Figure 4: Deformation contour for validation case by NOSBPD (solid line), compared with the results obtained by MPM method (dot-dash line) and also physical experiment (dashed line) at (a) t = 40 ms; (b) t = 80 ms; (c) t = 320 ms and physical experiment results by Shi et al. (2018) at (d) t = 40 ms; (e) t = 80 ms; (f) t = 320 ms.

to earthquake loading, which is exerted as body forces in the direction of x-axis. The boundary settings are consistent with the landslide large-deformation simulation studies conducted by Liu et al. (2022c) and Ren et al. (2023). More details about the mechanical parameters of soils are listed in Table 2. In this deterministic analysis and the following random field analysis, all the mechanical properties of soil except the soil cohesive strength are set uniformly all across the domain. In dynamic analysis, the determination of the minimum time step is crucial for the entire computation process. Smaller time steps enhance computational precision and contribute to the convergence of the model's calculations. In this study, the minimum time step is determined following the Courant–Friedrichs–Levy condition (Bui et al., 2008), set at 1.2×10^{-3} seconds, and the output data is extracted every 500 steps. In the current research, our model operates in a two-dimensional (2D) context. This is the first step that facilitates a 2D analysis as a basic solution, solving the key utilization of the novel method. It is imperative to highlight that our future research endeavors will encompass the extension of this methodology to 3D analysis.

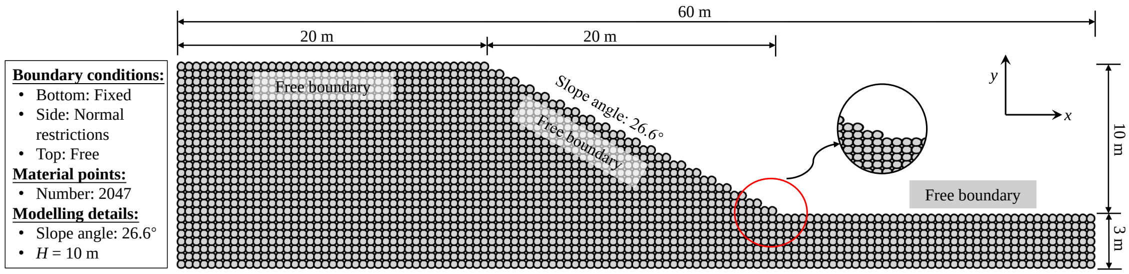

Figure 5: Geometry and boundary conditions of analyzed soil slope model.

Table 2: Soil mechanical parameters and modeling information.

Mechanical parameter	Symbol	Unit	Value
a. Deterministic analysis			
Density	ρ	g/cm^3	2.5
Young's modulus	E	MPa	30
Poisson's ratio	μ	-	0.25
Dilation angle	ψ	$^\circ$	0
Friction angle	φ	$(^\circ)$	15
Cohesion	c	kPa	5
Slope height	H	m	10
Slope angle	α	$^\circ$	26.6
Input peak ground acceleration	PGA	g	$0.2g; 0.3g; 0.4g; 0.5g$
b. Statistical properties of lognormal random field for c of heterogeneous soils			
Mean average of cohesion	c_{a}	kPa	5
Coefficient of variation	$\mathrm{CoV}_{\mathrm{RF}}$	-	0.2; 0.5
Horizontal correlation length	Θ_x	m	20
Vertical correlation length	Θ_y	m	4

2.7. Input ground motions

In order to ensure that the input ground motions exhibit a pulse-like velocity profile and adhere to the specified seismic criteria, the artificial ground motion simulation process diligently regulates both time-domain and frequency-domain characteristics for pulse-like ground motions (PLGMs). This regulation is achieved through the application of amplitude modulation functions and the alignment with target spectra (Chen et al., 2023). Consequently, it is plausible that the associated uncertainty in these simulations is underestimated when compared to natural seismic records.

To further investigate the influence of near-fault PLGMs on landslides, PLGM records and NPGM records from the PEER NGA-West2 database based on earthquake magnitude and proximity criteria were selected. The specific selection criteria for recorded PLGMs are as follows: the moment magnitude greater than 6 Mw, a rupture distance less than 20 km, and a peak ground velocity (PGV) exceeding 80 cm/s. We have identified a total of thirty PLGMs meeting these stringent criteria. In alignment, we have selected thirty NPGMs with comparable magnitudes and rupture distances. Horizontal seismic excitations have been considered for these selections. The detailed list of the chosen ground motions is presented in Table 3, with comprehensive insights into the ground motion selection process available in the work by Mo et al. (2022).

Table 3: PLGMs and NPGMs from PEER NGA-West2

No.	RSN (P)	RSN (NP)	No.	RSN (P)	RSN (NP)	No.	RSN (P)	RSN (NP)
1	171	160	11	1084	949	21	4847	5262
2	180	162	12	1085	1048	22	6906	5656
3	181	165	13	1120	1513	23	6911	8063
4	182	284	14	1244	1521	24	6927	8118
5	723	727	15	1492	1535	25	6962	8157
6	828	728	16	1503	1549	26	1119	1495
7	879	741	17	1510	1787	27	1505	1611
8	1044	753	18	2114	4457	28	1529	4013
9	1045	765	19	3548	4865	29	8119	8165
10	1063	848	20	4040	4886	30	8123	8166

Note: RSN denotes record sequence number; RSN (P) and RSN (NP) represent the RSN code of PLGMs and NPGMs from PEER NGA-West2 flatfile, respectively.

2.8. Simulation of heterogeneous soils

The characteristic strength of soil can be described by cohesion parameter c. Briefly, the spatial variability of soil has been verified through field investigations and laboratory tests (Wang et al., 2021c). The log-normal distributed random field of cohesion is commonly adopted to depict the spatial variability of soil as many scholars did (see Ouyang et al., 2021; Wang et al., 2021b). Hence, the log-normal distributed cohesion random field is generated by modified linear estimation method (MLE) (Liu et al., 2014) in the current study. To begin with, a spatially continuous and stationary Gaussian random field is generated following the steps provided by the MLE method. That is, we generate a stationary $G(x, y)$ with squared exponential autocorrelation function $\rho(x, y)$

as,

$$\rho(x,y) = \exp\left\{-\pi(\frac{\Delta x}{\Theta_x})^2 - \pi(\frac{\Delta y}{\Theta_y})^2\right\} \tag{47}$$

where Θ_x and Θ_y are the scales of fluctuation along x-, y-directions; Δx and Δy represent the difference in absolute distance between two points along $x-$ and $y-$directions. Then, exponential transformation is conducted to transfer the generated Gaussian random field into log-normal random field. Due to the computation approach adopted in this study, we simplify our consideration by neglecting the anisotropy of every single material point and directly assigning the generated random field values to every material point. The specific parameters of the generated cohesive strength random field are presented in Table 2. In this context, our study considers a mean value of 5 kPa for cohesion (c_{mean}, with two distinct cases for coefficient of variation (CoV), denoted as 0.2 and 0.5. Conversely, in the case of homogeneous soil, a fixed value of 5 kPa for cohesion is employed for deterministic analysis.

3. Results and discussions

3.1. Entire process of landslides with homogeneous soils

Figure 6 illustrates the entire process from the initiation to the failure of horizontal run-out distance of landslide in homogeneous soils subjected to a typical ground motion NPGM RSN 162 with PGA = 0.3g. The velocity (v), acceleration (a), 5% damped spectral acceleration (S_a) and Fourier spectrum (E_f) of typical NPGM RSN 162 are illustrated in Figure 7. Note that the simulations were carried out with a two-step process. The geostress equilibrium was established first, followed by the application of seismic loads. In the presented results, it can be observed that the run-out will happen at the foot of the slope accompanied with subsidence at the top of the slope simultaneously when subjected to seismic loading. With the earthquake going on, the extent of both subsidence at the slope's top and the displacement of soil particles at its foot progressively intensify.

Figure 6 (a) shows the change of horizontal displacement during the entire process of landslide. When $t = 6$s, under the influence of a significant seismic load, the initiation of the sliding surface on the slope has begun. By $t = 10$s, still subjected to a substantial seismic load, the sliding surface on the slope has further expanded, and the horizontal run-out distance continues to increase. As we reach $t = 20$s, the seismic load has reduced to extremely low amplitudes, essentially coming to a halt. At this point, the horizontal run-out distance is now twice that of the sixth second, and the slope continues to slide under the effect of inertia forces. Nevertheless, the rate of horizontal run-out distance increase decelerates as a result of the soil's shear resistance. At $t = 38$s, the seismic load has ceased entirely, and the calculations have finally converged. It is important to acknowledge that the run-out distances of this research may differ from those of other researchers, such as Feng et al. (2021). These discrepancies can be attributed to the variations of of soil properties and ground motion types.

In addition, NOSBPD offers a significant advantage in the present study due to its capacity to effectively address substantial deformations and the post-failure behavior of soil. As depicted in Figure 6 (b), the final slope configuration following collapse is illustrated. Notably, NOSBPD excels in simulating the extensively discontinuous failures along potential slip surfaces within the soil, a task that proves challenging for FEM. In the simulation by NOSBPD, the observed failure pattern in the slope corresponds to a 'toe failure' pattern. In contrast to the extensive sliding surface obtained by FEM, the sliding surface is clearly visible by NOSBPD, which yields a narrower and more localized shear band. Another intriguing observation lies in the realm of NOSBPD, where we can discern that particles, subjected to seismic loading, accumulate at the base of the slope due to being expelled under pressure, resulting in a 'pile-up' effect.

Moreover, in this study, the influence of the magnitude of PGA values on the horizontal run-out distance of the slope under a single input ground motion is also investigated. Figure 8 illustrated the final termination horizontal run-out displacement and plastic strain contours under various values of input ground motion PGA including $0.2g, 0.3g, 0.4g$ and $0.5g$. By comparing the horizontal run-out distances at different PGA values, it can be observed that prior to reaching 0.4g in loading, the run-out distance exhibits a roughly linear increase, while after reaching 0.4g, the rate of increase decreases slightly. The decrease in the rate of increase is likely due to the pronounced nonlinearity of the soil. Under seismic loading with higher PGA values, it is possible that the pile-up effect at the base of the slope could lead to a more substantial increase in the horizontal run-out distance, creating an impediment.

Note that all computations were performed on a computer equipped with an Intel(R) Core(TM) i7-9700 CPU running at 3.00 GHz. The computational process for a single run required approximately 15 minutes. Computers boasting higher performance specifications are anticipated to yield even shorter computation time. Despite our relatively modest computer setup, it is worth emphasizing that our computation time is still considerably shorter in comparison to the use of

Eulerian-Lagrangian finite element methods (on a high-end computer configuration), as cited in Chen et al.'s report (Chen et al., 2021). Also, to enhance computational speed and efficiency, the inclusion of CPU parallelization may be considered in the upcoming phases of this work.

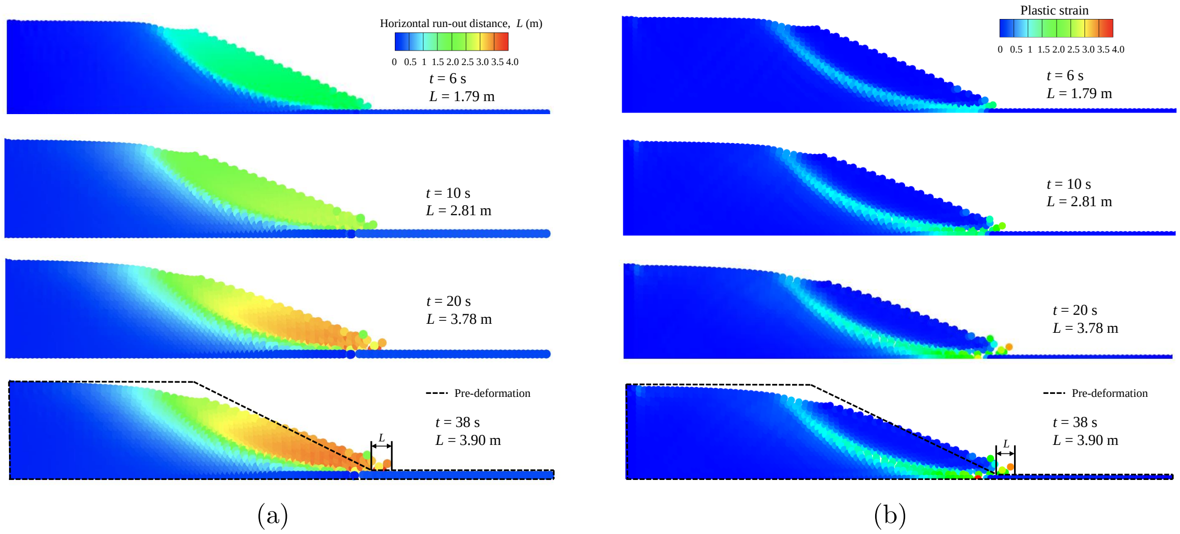

Figure 6: Horizontal run-out distance and plastic strain contours of landslide from initiation to termination within homogeneous soil under NPGM RSN 162 with PGA = 0.3g. (a) Horizontal run-out displacement contours; (b) plastic strain contours.

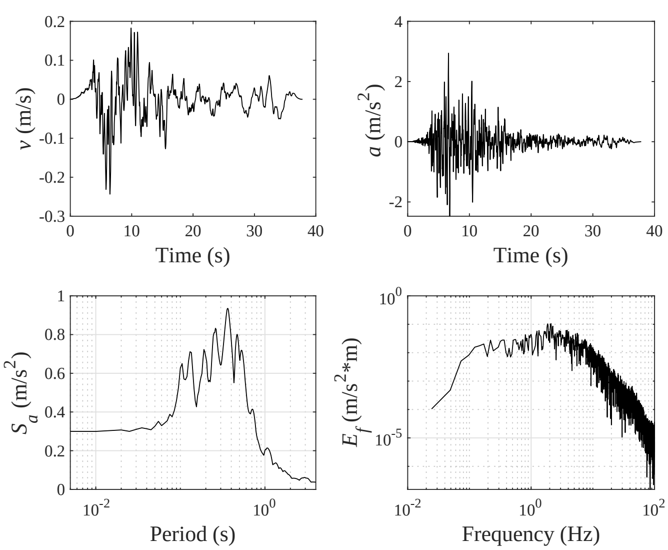

Figure 7: Velocity (v), acceleration (a), 5% damped spectral acceleration (S_a) and Fourier spectrum (E_f) of typical NPGM RSN 162.

3.2. Effects of ground motions

The ground motions play a pivotal role in the entire landslide process. However, previous studies on large deformations have generally overlooked the investigation of ground motion types

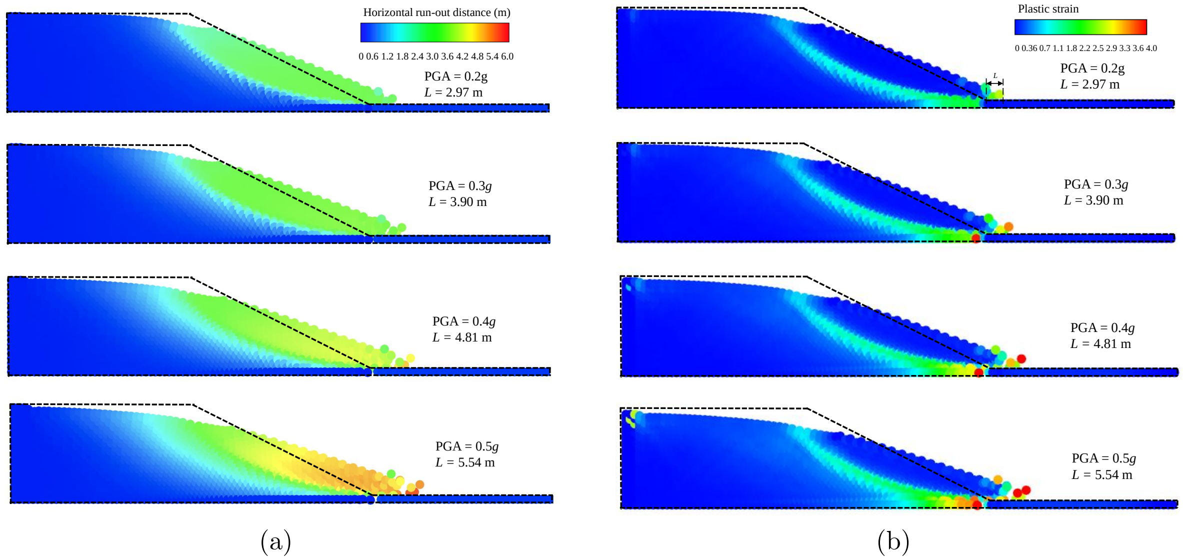

Figure 8: Final termination horizontal run-out displacement and plastic strain contours with various values of input ground motion PGA. (a) Horizontal run-out displacement contours; (b) plastic strain contours.

(e.g., Liu et al., 2022c). In fact, in the majority of existing research, ground motions are solely represented by PGA. Therefore, based on the NOSBPD algorithm, we aim to compare the destructive effects of two types of input ground motions, namely, NPGMs and PLGMs, on landslides. As described in Section 2.7, we utilize recorded ground motions to avoid underestimating the associated uncertainties resulting from the use of artificial ground motions (the artificial ground motion simulations rigorously adjust the time-domain and frequency-domain characteristics of PLGMs, which may lead to a certain degree of neglect of relevant uncertainties during the amplitude modulation process). The statistical results for the calculation of the final horizontal run-out distance in homogeneous soil for both types of input ground motions, with 30 instances each, are depicted in Figure 9 (a). It is evident from the boxplot that under PLGM loading, both the overall and mean values of the final horizontal run-out distance are greater than the results obtained with NPGM, approximately 1.2 times higher. That is, compared to NPGM, PLGM is found to induce more severe landslides. Figure 9 (b) illustrates the scatter of horizontal run-out distance values induced by two types of input ground motions. It is evident from the scatter that both NPGM-induced and PLGM-induced results exhibit a similar range in the magnitudes of their maximum and minimum horizontal sliding distances. NPGM-induced results fluctuate within a relatively smaller overall numerical range, while PLGM-induced results display higher numerical values overall. The maximum values are attributed to PLGM-induced events, whereas the minimum values are linked to NPGM-induced events. Moreover, in terms of data dispersion, NPGM-induced data exhibits a greater degree of variability when compared to the data associated with PLGMs. This suggests that PLGM-induced landslides not only have larger run-out distances but also a more concentrated distribution, implying a higher probability of PLGM-induced landslide occurrences.

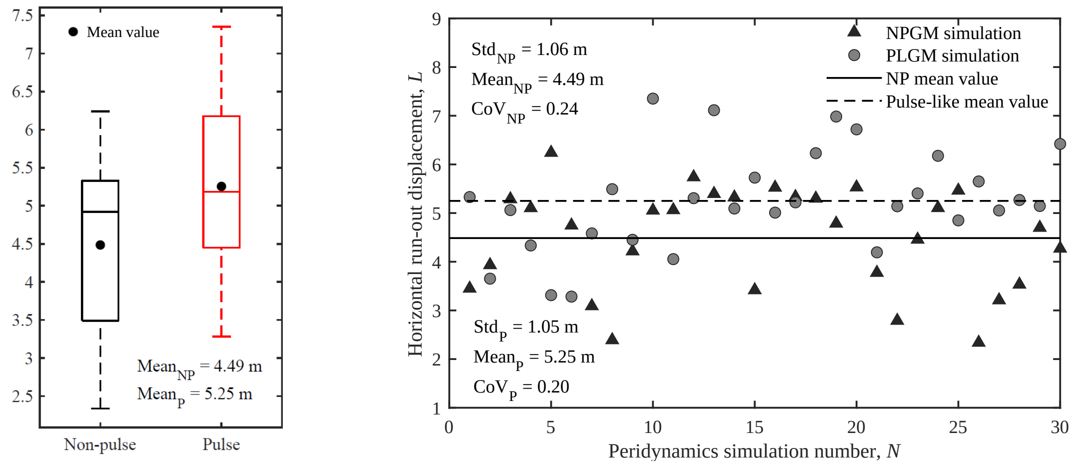

(a) (b)

Figure 9: Boxplot and scatter of horizontal run-out displacement (Unit: m) in homogeneous soils subjected to NPGMs and PLGMs.

3.3. Effects of soil heterogeneity

To control the variables involved, typical input ground motion RSN 162, as shown in Figure 7, were utilized as seismic loads in this section. A total of 100 random fields were generated through the MLE method for Monte Carlo simulations. Furthermore, in order to investigate the degree of soil heterogeneity, this section primarily focuses on two scenarios of random field parameters with $\mathrm{CoV_{RF}}$ values set at 0.2 and 0.5, allowing for a comparative analysis.

Figure 10 displays a representative sample generated using the random field parameters from Table 2, with a $\mathrm{CoV_{RF}}$ of 0.2. The diagram illustrates the interconnection of three clouds with relatively low cohesion (Figure 10 (a)). Following the application of seismic loading, this specific area exhibits diminished shear resistance, ultimately resulting in the formation of a sliding plane (see Figure 10 (b)). This is also the reason why the final horizontal run-out distance obtained from this random sample is greater than the horizontal run-out distance of uniform soil. The latter overlooks the contribution of the weaker soil layers resulting from soil heterogeneity in facilitating the formation of the slope sliding surface.

Figure 11 provides a more detailed entire process simulation of the landslide occurring in this random sample. The entire process of a slope landslide with heterogeneous soils, analogous

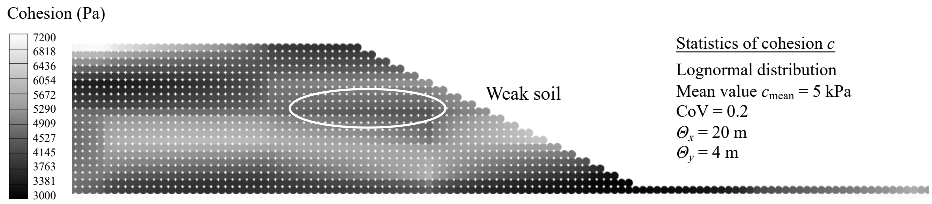

(a)

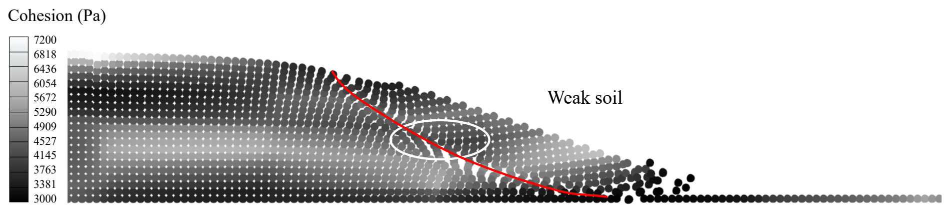

(b)

Figure 10: Typical realization of cohesion random field. (a) Initial state; (b) final state.

to deterministic analysis of landslide processes, follows a similar pattern. Initially, there is a formation of depression at the slope, followed by an overflow of soil particles at the toe of the slope. Under the sustained loading of seismic loads, the slope progressively diminishes its shear strength, culminating in a landslide event. What sets it apart from deterministic analysis is that, in terms of run-out distance, the homogeneous slope exhibits a run-out distance of 1.79 meters at the 6-th second (see Figure 6), as opposed to the 2.46 meters observed in the inhomogeneous soil slope, representing a 1.4-fold increase. This is under conditions with a $\mathrm{CoV}_{\mathrm{RF}}$ of 0.2. By the 10th second, the heterogeneous slope has already slid approximately 3.6 meters, approaching the run-out distance observed in the homogeneous slope after 20 seconds of loading. That is, the heterogeneity of soil distributed within the typical random sample accelerates the slope landslide process.

Figure 12 presents statistical data results for the horizontal run-out distance from Monte Carlo simulations. To illustrate the convergence of the Monte Carlo simulation results as the number of simulations increases, the convergence processes for two cases are depicted in Figure 13. It is evident that for a random field parameter with a $\mathrm{CoV}_{\mathrm{RF}}$ of 0.2, the average run-out distance when considering soil heterogeneity is 4.00 m, whereas the run-out distance for homogeneous soil is 3.90 m. For a random field parameter with a $\mathrm{CoV}_{\mathrm{RF}}$ of 0.5, the average horizontal run-out distance when considering soil heterogeneity is 4.35 m, representing a 12% increase compared to deterministic analysis. That is, neglecting the spatial variability of the soil can lead to an underestimation of the landslide run-out distance.

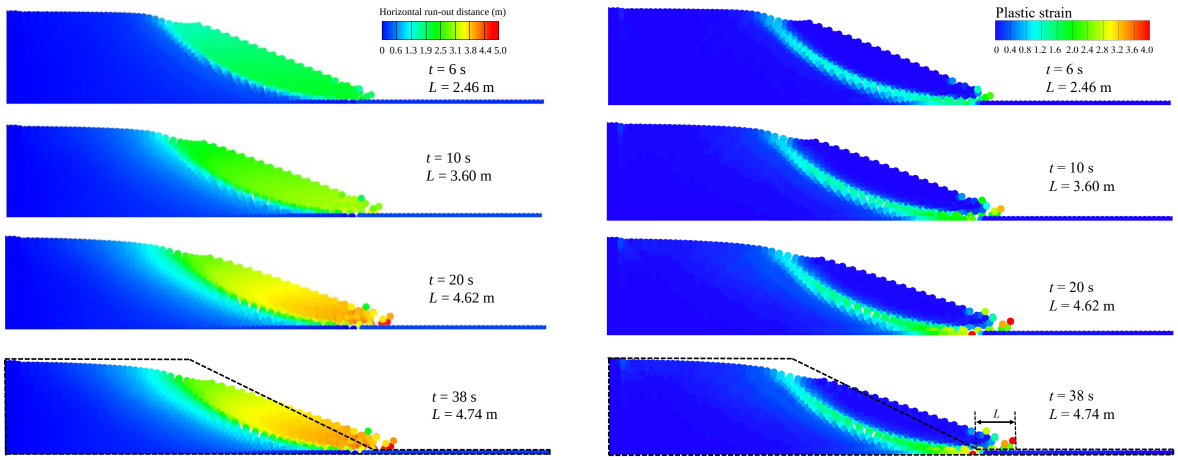

(a) (b)

Figure 11: Typical landslide process within heterogeneous soils following distribution in Figure 10. (a) Horizontal run-out distance contours; (b) plastic strain contours.

Table 4: Statistical results accounting for multiple sources of uncertainty

Scenario	Trigger	CoV Value
Considering input ground motion types	NPGMs	0.24
	PLGMs	0.20
Considering soil heterogeneity	$\mathrm{CoV_{RF}} = 0.2$	0.11
	$\mathrm{CoV_{RF}} = 0.5$	0.22

To clarify, the simulation results for two different sets of random field parameters show that when $\mathrm{CoV_{RF}}$ is 0.2, the simulation data has a CoV of 0.11, whereas when $\mathrm{CoV_{RF}}$ is 0.5, the simulation data has a CoV of 0.22. This means that an increase in the degree of soil spatial variability leads to a significantly higher level of variability in the landslide run-out distance data, approximately doubling it. Moreover, when considering the influence of two types of ground motions (Section 3.2), the resulting data has a CoV of 0.24 for NPGMs (i.e., $\mathrm{CoV_{NP}} = 0.24$) and has a CoV of 0.20 for PLGMs (i.e., $\mathrm{CoV_{P}} = 0.20$), two values very close to the CoV obtained when the random field parameter $\mathrm{CoV_{RF}}$ is set to 0.5, as listed in Table 4. This implies that in this scenario, the impact of soil spatial variability and the type of input ground motion on the landslide process is quite comparable. Therefore, both soil spatial variability and the type of input ground motion play crucial roles in landslide process.

3.4. Coupling effects of ground motion and soil heterogeneity

In this section, to investigate the coupling effects of ground motion and soil heterogeneity and to ensure the representativeness of data, spatially variable samples with $\mathrm{CoV_{RF}} = 0.5$ have been

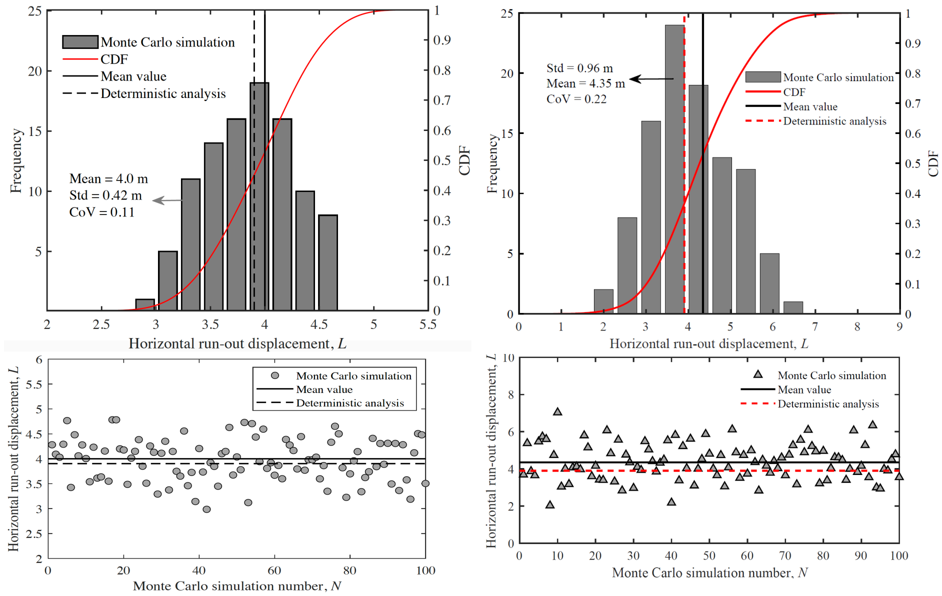

(a) (b)

Figure 12: Histogram and scatter of horizontal run-out displacement (Unit: m) subjected to NPGM RSN 162 in heterogeneous soil with random field parameter (a) $\mathrm{CoV_{RF}} = 0.2$; (b) $\mathrm{CoV_{RF}} = 0.5$.

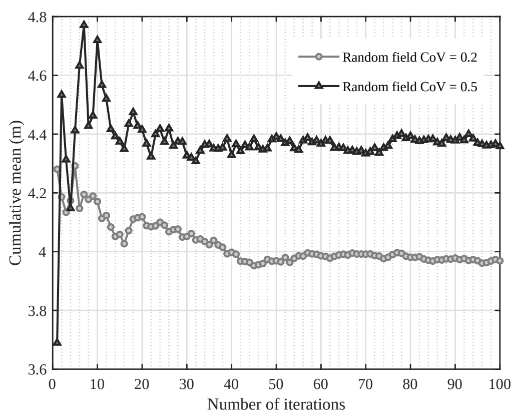

Figure 13: Convergence plot as Monte Carlo iterations increase.

chosen that closely approximate the mean values of Monte Carlo simulations. This selection is based on the results obtained in Section 3.4. Also, based on the results illustrated in Section 3.2, which indicated a higher level of variability in NPGMs. Hence, NPGM type of ground motion has been selected as the input ground motion. The top 25 NPGMs (as presented in Table 3) were chosen for analysis. The objective here is to examine whether ground motion randomness amplifies this level of variability for soil heterogeneity.

One hundred Monte Carlo simulations were performed, and the resulting run-out distances are illustrated in Figure 14 (a). The scatter indicates that both mean value and CoV value have increased. The mean value of run-out distances is 4.90 m, representing an increase of 8.4%

when compared to the computed results for homogeneous soil (Mean value = 4.49 m). Also, the scatter reveals that the dispersion of the obtained run-out distance values (CoV = 0.25) exhibits a slight increase when compared to the results in homogeneous soil (CoV = 0.24, see Figure 9 (b)). This difference is relatively minor which attributed to the deliberate control of soil uncertainty. Nonetheless, in Figure 14 (b), it is still evident that the spatial variability of the soil under different seismic waves is amplified to varying degrees, particularly for RSN 949, RSN 1535, and RSN 5262. Notably, the CoV value for RSN 1535 reaches 0.135. In other words, different ground motions lead to varying degrees of amplification in the spatial variability of the soil, resulting in increased variability compared to considering uncertainty from a single source alone. The mechanism behind the amplification of soil spatial variability by ground motion will be a part of future research. This underscores the necessity of considering the coupling effect of these two sources of uncertainty in earthquake-induced landslide risk assessment.

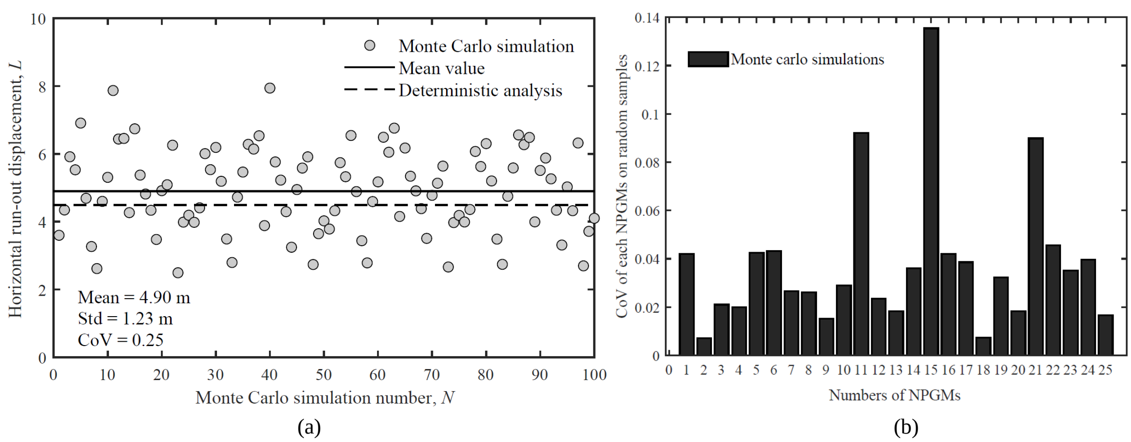

Figure 14: Coupling effects of ground motion and soil heterogeneity. (a) Scatter of Monte Carlo simulations; (b) histogram of CoV value of each NPGMs on random samples.

4. Conclusions

In this study, we proposed a computational method to analyze the entire process of slope run-out by utilizing the features of PD. Moreover, we performed NOSBPD modelling on large-deformation landslide processes in random soils subjected to stochastic ground motions. Parametric studies were conducted to explore the impacts of spatial variability of soils, input ground motions types, and coupling effects on entire process and failure mechanism of earthquake-induced landslides. The conclusions can be summarized as follows.

(1) The effectiveness of modeling large-deformation landslide processes based proposed computational method was investigated by numerical case studies. The results have indicated that PD is a promising and reliable method for simulating large-deformation phenomena. In comparison to mesh-based methods, PD offers the capability to simulate discontinuous soil failure, capturing the entire process of slope landslides while providing a more localized representation of shear bands.

(2) Moreover, we introduced random field theory into PD and proposed a coupling procedure. By doing so, the varying degrees of heterogeneous spatial variability in soil strength and its effects on landslide behavior were investigated. For a random field parameter with a coefficient of variation of 0.5, the average horizontal run-out distance, when considering soil heterogeneity, was found to be 4.35 meters. This represents a 12% increase compared to homogeneous soil analyses, highlighting the importance of accounting for spatial variability in soil properties to avoid underestimating landslide run-out distances.

(3) Recognizing the significant impact of input ground motions on landslides, this study deliberately examined the influence of two distinct types of seismic motions, namely NPGMs and PLGMs, on the landslide process. The findings suggest that landslides under PLGMs not only exhibit statistically larger run-out distances but also smaller variation, implying a higher likelihood of landslides under PLGMs.

(4) The extent to which the individual and coupling effects of ground motion types and spatial variability affect earthquake-induced landslides was explored. The results indicate that both uncertainty sources exert significant influences on landslide behavior. Neglecting the uncertainties stemming from both sources can lead to an underestimation of the landslide run-out risk. Furthermore, the necessity of considering the coupling effect of these two sources of uncertainty in earthquake-induced landslide risk assessment.

Acknowledgements

This research is supported by the National Natural Science Foundation of China (Grant No. U22A20596) and the Natural Science Foundation Innovation Group Project of Hubei Province, China (Grant No. 2023AFA017). Ruohan Wang has received financial support from China Scholarship Council (CSC No. 202206270125).

Appendix. Convergence analysis on material point number

The number of material points can have a certain range of impact on computational results; however, a larger number of material points concurrently escalates computational costs. In order to rigorously examine this influence, we conducted a convergence analysis on material point number to demonstrate that the adopted quantity of material points in this study is sufficient to attain convergent results. Here, we employed five different ratios of area to the number of material points (e) for simulation, namely 20%, 24%, 40%, 55%, and 100%. They correspond to material point numbers (β) of 2369, 2047, 1201, 925, respectively.

In Figure 15, as the ratio e decreases from 100% to 20%, corresponding to an increase in β from 925 to 2369, the horizontal run-out displacement (L) gradually increases, ultimately converging to 3.5 m. Figure 16 depicts distributions of plastic strain for the five different e ratios. It is observed that the thickness of the shear band decreases with an increase in the number of material points and remains nearly constant after the e ratio drops to 24%. Between e ratios of 24% and 20%, there is no significant difference in horizontal run-out displacement and shear band thickness. Therefore, the adopted number of material points in this study is sufficient to achieve convergent results.

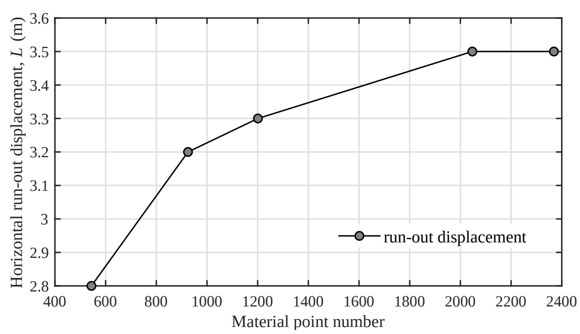

Figure 15: Convergence analysis on material point number β for horizontal run-out displacement L.

References

Akram, S., Ann, Q.U., 2015. Newton Raphson method. International Journal of Scientific & Engineering Research 6 (7), 1748–1752.

Baker, J.W., 2007. Quantitative classification of near-fault ground motions using wavelet analysis. Bulletin of the Seismological Society of America 97 (5), 1486–1501.

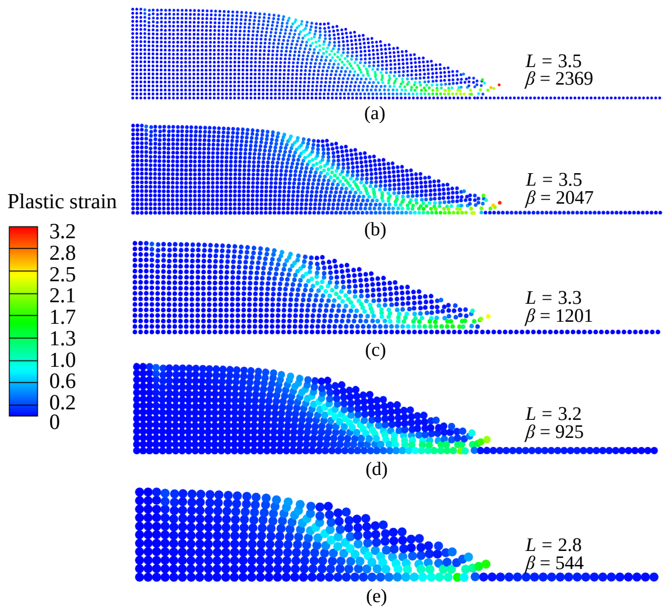

Figure 16: Plastic strain distributions calculated with various material point numbers β: (a) $\beta = 2369$; (b) $\beta = 2047$ (this study); (c) $\beta = 1201$; (d) $\beta = 925$; (e) $\beta = 544$.

Bathe, K.J., Ramm, E., Wilson, E.L., 1975. Finite element formulations for large deformation dynamic analysis. International Journal for Numerical Methods in Engineering 9 (2), 353–386.

Bergel, G.L., Li, S., 2016. The total and updated lagrangian formulations of state-based peridynamics. Computational Mechanics 58, 351–370.

Bishop, A.W., 1955. The use of the slip circle in the stability analysis of slopes. Géotechnique 5 (1), 7–17.

Bobaru, F., Foster, J.T., Geubelle, P.H., Silling, S.A., 2016. Handbook of peridynamic modeling. CRC press.

Breitenfeld, M.S., Geubelle, P.H., Weckner, O., Silling, S., 2014. Non-ordinary state-based peridynamic analysis of stationary crack problems. Computer Methods in Applied Mechanics and Engineering 272, 233–250.

Breitzman, T., Dayal, K., 2018. Bond-level deformation gradients and energy averaging in peridynamics. Journal of the Mechanics and Physics of Solids 110, 192–204.

Bui, H.H., Fukagawa, R., Sako, K., Ohno, S., 2008. Lagrangian meshfree particles method (SPH) for large deformation and failure flows of geomaterial using elastic-plastic soil constitutive model.

International Journal for Numerical and Analytical Methods in Geomechanics 32 (12), 1537–1570.

Bui, H.H., Ryoichi, F., Kazunari, S., Craig, W.J., 2011. Slope stability analysis and discontinuous slope failure simulation by elasto-plastic smoothed particle hydrodynamics (SPH). Géotechnique 61 (7), 565–574.

Bui, H.H., Sako, K., Fukagawa, R., 2007. Numerical simulation of soil–water interaction using smoothed particle hydrodynamics (SPH) method. Journal of Terramechanics 44 (5), 339–346.

Chen, G., Yang, J., Wang, R., Li, K., Liu, Y., Beer, M., 2023. Seismic damage analysis due to near-fault multipulse ground motion. Earthquake Engineering & Structural Dynamics 52 (15), 5099–5116.

Chen, H., 2018. Bond-associated deformation gradients for peridynamic correspondence model. Mechanics Research Communications 90, 34–41.

Chen, H., Hu, X., 2023. Influence functions for accurate representation of bond deformation in discrete modeling. Mechanics Research Communications 134, 104220.

Chen, X., Li, D., Tang, X., Liu, Y., 2021. A three-dimensional large-deformation random finite-element study of landslide runout considering spatially varying soil. Landslides 18 (9), 3149–3162.

Corominas, J., van Westen, C., Frattini, P., Cascini, L., Malet, J.P., Fotopoulou, S., Catani, F., Van Den Eeckhaut, M., Mavrouli, O., Agliardi, F., et al., 2014. Recommendations for the quantitative analysis of landslide risk. Bulletin of Engineering Geology and the Environment 73, 209–263.

Fan, H., Bergel, G.L., Li, S., 2016. A hybrid peridynamics–SPH simulation of soil fragmentation by blast loads of buried explosive. International Journal of Impact Engineering 87, 14–27.

Fan, Z., Zheng, H., Lin, S., 2021. Shear band static evolution by spatially mobilized plane criterion based drucker-prager model and numerical manifold method. Computers and Geotechnics 132, 103962.

Fellenius, W., 1936. Calculation of the stability of earth dams, in: Proc. of the second congress on large dams, pp. 445–463.

Feng, K., Wang, G., Huang, D., Jin, F., 2021. Material point method for large-deformation modeling of coseismic landslide and liquefaction-induced dam failure. Soil Dynamics and Earthquake Engineering 150, 106907.

Ghosh, S., Kikuchi, N., 1991. An arbitrary lagrangian-eulerian finite element method for large deformation analysis of elastic-viscoplastic solids. Computer Methods in Applied Mechanics and Engineering 86 (2), 127–188.

Gingold, R.A., Monaghan, J.J., 1977. Smoothed particle hydrodynamics: theory and application to non-spherical stars. Monthly Notices of the Royal Astronomical Society 181 (3), 375–389.

Griffiths, D., Fenton, G.A., 2004. Probabilistic slope stability analysis by finite elements. Journal of Geotechnical and Geoenvironmental Engineering 130 (5), 507–518.

Hicks, M.A., Li, Y., 2018. Influence of length effect on embankment slope reliability in 3D. International Journal for Numerical and Analytical Methods in Geomechanics 42 (7), 891–915.

Housner, G.W., Hudson, D.E., 1958. The Port Hueneme earthquake of March 18, 1957. Bulletin of the Seismological Society of America 48 (2), 163–168.

Hu, Y., Randolph, M., 1998. A practical numerical approach for large deformation problems in soil. International Journal for Numerical and Analytical Methods in Geomechanics 22 (5), 327–350.

Huang, Y., Li, G., Xiong, M., 2020. Stochastic assessment of slope failure run-out triggered by earthquake ground motion. Natural Hazards 101, 87–102.

Janbu, N., 1968. Slope stability computations, soil mechanics and foundation engineering report. Technical University of Norway, Trondheim .

Kan, X., Yan, J., Li, S., Zhang, A.M., 2021. On differences and comparisons of peridynamic differential operators and nonlocal differential operators. Computational Mechanics 68, 1349–1367.

Kularathna, S., Soga, K., 2017. Comparison of two projection methods for modeling incompressible flows in MPM. Journal of Hydrodynamics, Ser. B 29 (3), 405–412.

Lai, X., Liu, L.S., Liu, Q.W., Cao, D.F., Wang, Z., Zhai, P.C., 2015. Slope stability analysis by peridynamic theory. Applied Mechanics and Materials 744, 584–588.

Li, P., Hao, Z., Zhen, W., 2018. A stabilized non-ordinary state-based peridynamic model. Computer Methods in Applied Mechanics and Engineering 339, 262–280.

Li, P., Liu, S., Ji, J., Ding, X., Bao, M., 2023. Stochastic analysis of excavation-induced wall deflection and box culvert settlement considering spatial variability of soil stiffness. Journal of Rock Mechanics and Geotechnical Engineering .

Liu, K., Vardon, P., Hicks, M., 2018. Sequential reduction of slope stability uncertainty based on temporal hydraulic measurements via the ensemble kalman filter. Computers and Geotechnics 95, 147–161.

Liu, K., Wang, Y., Huang, M., Yuan, W.H., 2021. Postfailure analysis of slopes by random generalized interpolation material point method. International Journal of Geomechanics 21 (3), 04021015.

Liu, L., Zhang, P., Zhang, S., Li, J., Huang, L., Cheng, Y., Wang, B., 2022a. Efficient evaluation of run-out distance of slope failure under excavation. Engineering Geology 306, 106751.

Liu, W.K., Li, S., Park, H.S., 2022b. Eighty years of the finite element method: Birth, evolution, and future. Archives of Computational Methods in Engineering 29 (6), 4431–4453.

Liu, X., Wang, Y., 2021. Probabilistic simulation of entire process of rainfall-induced landslides using random finite element and material point methods with hydro-mechanical coupling. Computers and Geotechnics 132, 103989.

Liu, Y., Chen, X., Hu, M., 2022c. Three-dimensional large deformation modeling of landslides in spatially variable and strain-softening soils subjected to seismic loads. Canadian Geotechnical Journal 60 (4), 426–437.

Liu, Y., Lee, F.H., Quek, S.T., Beer, M., 2014. Modified linear estimation method for generating multi-dimensional multi-variate gaussian field in modelling material properties. Probabilistic Engineering Mechanics 38, 42–53.

Lucy, L.B., 1977. A numerical approach to the testing of the fission hypothesis. Astronomical Journal 82, 1013–1024.

Madenci, E., Barut, A., Futch, M., 2016. Peridynamic differential operator and its applications. Computer Methods in Applied Mechanics and Engineering 304, 408–451.

Mavroeidis, G.P., Papageorgiou, A.S., 2003. A mathematical representation of near-fault ground motions. Bulletin of the Seismological Society of America 93 (3), 1099–1131.

Mo, T., Wu, Q., Li, D.Q., Du, W., 2022. Influence of ground motion characteristics (velocity pulse and duration) on the pile responses in liquefiable soil deposits. Soil Dynamics and Earthquake Engineering 159, 107330.

Mohajerani, S., Wang, G., 2022. "Touch-aware" contact model for peridynamics modeling of granular systems. International Journal for Numerical Methods in Engineering 123 (17), 3850–3878.

Morgenstern, N.R., Price, V.E., 1965. The analysis of the stability of general slip surfaces. Géotechnique 15 (1), 79–93.

Ouyang, J., Liu, Y., Yao, K., Yang, C., Niu, H., 2021. Model updating of slope stability analysis using 3D conditional random fields. ASCE-ASME Journal of Risk and Uncertainty in Engineering Systems, Part A: Civil Engineering 7 (3), 04021034.

Phoon, K., Kulhawy, F.H., 1999. Characterization of geotechnical variability. Canadian Geotechnical Journal 36 (4), 612–624.

Qu, C., Wang, G., Feng, K., Xia, Z., 2021. Large deformation analysis of slope failure using material point method with cross-correlated random fields. Journal of Zhejiang University-SCIENCE A (Applied Physics & Engineering) 22 (11), 856–869.

Ren, B., Li, S., 2012. Modeling and simulation of large-scale ductile fracture in plates and shells. International Journal of Solids and Structures 49 (18), 2373–2393.

Ren, S., Chen, X., Ren, Z.L., Cheng, P., Liu, Y., 2023. Large-deformation modelling of earthquake-triggered landslides considering non-uniform soils with a stratigraphic dip. Computers and Geotechnics 159, 105492.

Shi, B., Zhang, Y., Zhang, W., 2018. Analysis of the entire failure process of the rotational slide using the material point method. International Journal of Geomechanics 18 (8), 04018092.

Silling, S.A., 2000. Reformulation of elasticity theory for discontinuities and long-range forces. Journal of the Mechanics and Physics of Solids 48 (1), 175–209.

Silling, S.A., Epton, M., Weckner, O., Xu, J., Askari, E., 2007. Peridynamic states and constitutive modeling. Journal of Elasticity 88, 151–184.

Somerville, P.G., Smith, N.F., Graves, R.W., Abrahamson, N.A., 1997. Modification of empirical strong ground motion attenuation relations to include the amplitude and duration effects of rupture directivity. Seismological Research Letters 68 (1), 199–222.

Spencer, E., 1967. A method of analysis of the stability of embankments assuming parallel inter-slice forces. Géotechnique 17 (1), 11–26.

Staubach, P., Kimmig, I., Machaček, J., Wichtmann, T., Triantafyllidis, T., 2023. Deep vibratory compaction simulated using a high-cycle accumulation model. Soil Dynamics and Earthquake Engineering 166, 107763.

Sulsky, D., Chen, Z., Schreyer, H.L., 1994. A particle method for history-dependent materials. Computer Methods in Applied Mechanics and Engineering 118 (1-2), 179–196.

Sulsky, D., Zhou, S.J., Schreyer, H.L., 1995. Application of a particle-in-cell method to solid mechanics. Computer Physics Communications 87 (1-2), 236–252.

Tupek, M.R., Radovitzky, R., 2014. An extended constitutive correspondence formulation of peridynamics based on nonlinear bond-strain measures. Journal of the Mechanics and Physics of Solids 65, 82–92.

Wang, B., Liu, L., Li, Y., Jiang, Q., 2020. Reliability analysis of slopes considering spatial variability of soil properties based on efficiently identified representative slip surfaces. Journal of Rock Mechanics and Geotechnical Engineering 12 (3), 642–655.

Wang, B., Vardon, P., Hicks, M., 2018a. Rainfall-induced slope collapse with coupled material point method. Engineering Geology 239, 1–12.

Wang, R., Li, D., Chen, E.J., Liu, Y., 2021a. Dynamic prediction of mechanized shield tunneling performance. Automation in Construction 132, 103958.

Wang, R., Li, D., Wang, M., Liu, Y., 2021b. Deterministic and probabilistic investigations of piping occurrence during tunneling through spatially variable soils. ASCE-ASME Journal of Risk and Uncertainty in Engineering Systems, Part A: Civil Engineering 7 (2), 04021009.

Wang, R., Sun, P., Li, D., Tyagi, A., Liu, Y., 2021c. Three-dimensional seepage investigation of riverside tunnel construction considering heterogeneous permeability. ASCE-ASME Journal of Risk and Uncertainty in Engineering Systems, Part A: Civil Engineering 7 (4), 04021041.

Wang, Y., Zhou, X., Kou, M., 2019. An improved coupled thermo-mechanic bond-based peridynamic model for cracking behaviors in brittle solids subjected to thermal shocks. European Journal of Mechanics-A/Solids 73, 282–305.

Wang, Y., Zhou, X., Wang, Y., Shou, Y., 2018b. A 3-D conjugated bond-pair-based peridynamic formulation for initiation and propagation of cracks in brittle solids. International Journal of Solids and Structures 134, 89–115.

Wang, Y., Zhou, X., Xu, X., 2016. Numerical simulation of propagation and coalescence of flaws in rock materials under compressive loads using the extended non-ordinary state-based peridynamics. Engineering Fracture Mechanics 163, 248–273.

Wicki, A., Lehmann, P., Hauck, C., Seneviratne, S.I., Waldner, P., Stähli, M., 2020. Assessing the potential of soil moisture measurements for regional landslide early warning. Landslides 17, 1881–1896.

Xu, Z., Stark, T.D., 2022. Runout analyses using 2014 Oso landslide. Canadian Geotechnical Journal 59 (1), 55–73.

Yaghoobi, A., Chorzepa, M.G., 2017. Higher-order approximation to suppress the zero-energy mode in non-ordinary state-based peridynamics. Computers & Structures 188, 63–79.

Ypma, T.J., 1995. Historical development of the Newton–Raphson method. SIAM Review 37 (4), 531–551.

Zeng, Z., Zhang, H., Zhang, X., Liu, Y., Chen, Z., 2022. An adaptive peridynamics material point method for dynamic fracture problem. Computer Methods in Applied Mechanics and Engineering 393, 114786.

Zhang, L., Liu, Y., 2020. Numerical investigations on the seismic response of a subway tunnel embedded in spatially random clays. Underground Space 5 (1), 43–52.

Zhang, P., Liu, L., Zhang, S., Cheng, Y., Wang, B., 2022. Material point method-based two-dimensional cohesive-frictional slope stability analysis charts considering depth coefficient effect. Bulletin of Engineering Geology and the Environment 81 (5), 206.

Zhang, T., Zhang, J., 2022. Numerical estimate of critical failure surface of slope by ordinary state-based peridynamic plastic model. Engineering Failure Analysis 140, 106556.

Zhou, X., Yao, W.W., Berto, F., 2021. Smoothed peridynamics for the extremely large deformation and cracking problems: Unification of peridynamics and smoothed particle hydrodynamics. Fatigue & Fracture of Engineering Materials & Structures 44 (9), 2444–2461.